The Astrophysical Journal, 774:10 (7pp), 2013 September 1 doi:10.1088/0004-637X/774/1/10
© 2013. The American Astronomical Society. All rights reserved. Printed in the U.S.A.

KINEMATICS OF SHOCKED MOLECULAR GAS ADJACENT TO THE SUPERNOVA REMNANT W44

Tomoro Sashida[1], Tomoharu Oka[1], Kunihiko Tanaka[1], Kazuya Aono[1],
Shinji Matsumura[1], Makoto Nagai[2], and Masumichi Seta[2]
[1] Department of Physics, Faculty of Science and Technology, Keio University, 3-14-1 Hiyoshi, Kohoku-ku, Yokohama, Kanagawa 223-8522, Japan
[2] Institute of Physics, University of Tsukuba, 1-1-1 Tennoudai, Tsukuba, Ibaraki 305-8571, Japan
Received 2013 April 21; accepted 2013 July 8; published 2013 August 8

ABSTRACT

We mapped molecular gas toward the supernova remnant W44 in the HCO^+ $J = 1$–0 line with the Nobeyama Radio Observatory 45 m telescope and in the CO $J = 3$–2 line with the Atacama Submillimeter Telescope Experiment 10 m telescope. High-velocity emission wings were detected in both lines over the area where the radio shell of W44 overlaps with the molecular cloud in the plane of the sky. We found that the average velocity distributions of the wing emission can be fit by a uniform expansion model. The best-fit expansion velocities are 12.2 ± 0.3 km s^{-1} and 13.2 ± 0.2 km s^{-1} in HCO^+ and CO, respectively. The non-wing CO $J = 3$–2 component is also fit by the same model with an expansion velocity of 4.7 ± 0.1 km s^{-1}. This component might be dominated by a post-shock higher-density region where the shock velocity had slowed down. The kinetic energy of the shocked molecular gas is estimated to be $(3.5 \pm 1.3) \times 10^{49}$ erg. Adding this and the energy of the previously identified H I shell, we conclude that $(1.2 \pm 0.2) \times 10^{50}$ erg has been converted into gas kinetic energy from the initial baryonic energy of the W44 supernova. We also found ultra-high-velocity CO $J = 3$–2 wing emission with a velocity width of ~ 100 km s^{-1} at $(l, b) = (+34.^\circ73, -0.^\circ47)$. The origin of this extremely high velocity wing is a mystery.

Key words: ISM: clouds – ISM: kinematics and dynamics – ISM: molecules – ISM: supernova remnants – radio lines: ISM

Online-only material: color figures

1. INTRODUCTION

The blast wave of a supernova (SN) explosion generates strong shocks in the interstellar medium, accelerating, compressing, and heating it, and forming a shell comprising the supernova remnant (SNR). At the same time, the blast wave releases an enormous baryonic energy of $E_{\rm bar} \sim 10^{51}$ erg. Until the end of its lifetime, most of the baryonic energy is converted to radiative energy, and thus only a small percentage of it remains as kinetic energy ($E_{\rm kin}$) of the interstellar matter (Chevalier 1974). Recent extragalactic studies have revealed that the conversion efficiency, $\eta \equiv E_{\rm kin}/E_{\rm bar}$, is $\sim$0.1 in quiescent star-forming galaxies, whereas it increases to $>$0.4 in starburst-like environments (Strickland & Heckman 2009).

The radio source W44 is a type II SNR with a distorted radio shell (e.g., Kundu & Velusamy 1972; Clark et al. 1975; Reich et al. 1984; Kassim 1992) and a center-filled X-ray morphology (e.g., Gronenschild et al. 1978; Smith et al. 1985; Rho et al. 1994; Harrus et al. 1997). It is located 3 kpc away from the Sun (e.g., Radhakrishnan et al. 1972; Caswell et al. 1975) and its estimated age is $(0.65$–$2.5) \times 10^4$ yr (e.g., Smith et al. 1985; Harrus et al. 1997). A giant molecular cloud (GMC) is associated with this SNR (Seta et al. 1998, 2004). The detection of OH 1720 MHz maser emission (Claussen et al. 1997; Frail & Mitchell 1998; Claussen et al. 1999), the enhanced CO $J = 2$–1/$J = 1$–0 ratio (Seta et al. 1998), and compact spots of high-velocity wing emission (Seta et al. 2004) are evidence of violent interaction between the molecular cloud and the W44 SNR. Extensive CO imaging has detected spatially extended, moderately broad emission (SEMBE), which might also be molecular gas disturbed by the SNR (Seta et al. 2004).

In this paper, we present extensive HCO^+ $J = 1$–0 and CO $J = 3$–2 maps of the W44 GMC (Section 3.1). The HCO^+ $J = 1$–0 line traces high-density [$n(H_2) \gtrsim 10^5$ cm^{-3}] gas, whereas CO $J = 3$–2 traces mainly warm moderate-density [$T_{\rm k} \geqslant 30$ K, $n(H_2) \gtrsim 10^{3.5}$ cm^{-3}] gas. We report the detection of faint, spatially extended wing emission in the HCO^+ $J = 1$–0 and CO $J = 3$–2 lines (Section 3.2). The kinematics of the shocked gas traced by the spatially extended wing emission are also presented. These data enable us to estimate the kinetic energy of the shocked molecular gas and consequently to estimate the total kinetic energy that has been supplied by the W44 SNR. We also report the discovery of ultra-high-velocity CO $J = 3$–2 wing emission (Section 3.3).

2. OBSERVATIONS

2.1. NRO 45 m

We mapped the W44 molecular cloud in the HCO^+ $J = 1$–0 line (89.1885 GHz) with the Nobeyama Radio Observatory (NRO) 45 m radio telescope in two ways. One way consisted of mapping a small area in the wide frequency band (512 MHz) mode. The objectives of this wide-band mapping were to confirm the detection of spatially extended HCO^+ wings and to investigate the spatial and velocity distribution of the shocked molecular gas. The other way consisted of extensive mapping in the narrow frequency band (32 MHz) mode. The objective here was to investigate the detailed kinematics of the shocked gas traced by HCO^+ wing emission.

In both mappings, the data were obtained with the 25 element focal plane receiver BEARS (Sunada et al. 2000). At 90 GHz, the telescope has an FWHM beam size of 18″ and a main-beam efficiency ($\eta_{\rm MB}$) of 44%. During these observations, the system noise temperatures ranged between 250 and 400 K in a double sideband. The antenna temperature was calibrated by the standard chopper-wheel method. Pointing errors were corrected

every 2 hr by observing the SiO maser source R Aql at 43 GHz. The pointing accuracy of the telescope was good to $\leqslant 3''$ in both azimuth and elevation. To correct the gain variation among the 25 beams of BEARS, we scaled the antenna temperature in each channel to that taken with the single-beam SIS receiver S100, which is equipped with a quasi-optical image rejection filter. A clean reference position of $(l, b) = (+33.^{\circ}750, -1.^{\circ}509)$ was chosen. We scaled the antenna temperature by multiplying by $1/\eta_{\rm MB}$ to obtain the main-beam temperature, $T_{\rm MB}$.

The wide-band HCO^+ mapping observations were conducted in 2007 May. The mapping area includes the group of OH 1720 MHz maser spots in the southwestern edge of the W44 radio shell (Claussen et al. 1997). The observations were performed by position switching to the clean reference position. We used 25 sets of 1024 channel autocorrelators (ACs) in the 512 MHz bandwidth mode, which has a 500 kHz resolution. At 90 GHz, these correspond to a 1700 km s^{-1} velocity coverage and a 1.7 km s^{-1} velocity resolution. The data were reduced using the NEWSTAR reduction package. We subtracted the baselines of the spectra by fitting linear lines. The data were smoothed with a Gaussian function and resampled onto a $17'' \times 17'' \times 1.0$ km s^{-1} regular grid. The rms noise level of the final map is 0.07 K in $T_{\rm MB}$ (1σ).

The extensive HCO^+ mapping was conducted from 2010 April to May. The mapping area completely covers the radio shell of W44. The observations were performed in the on-the-fly (OTF) mapping mode. We used ACs in the 32 MHz bandwidth mode, which has a 37.8 kHz resolution; these values correspond to a 107 km s^{-1} velocity coverage and a 0.1 km s^{-1} velocity resolution. The data were reduced using the NOSTAR reduction package. They were smoothed with a Bessel–Gaussian function and resampled onto a $17'' \times 17'' \times 1$ km s^{-1} regular grid. The rms noise level of the final map is 0.075 K in $T_{\rm MB}$ (1σ).

2.2. ASTE

We also observed the W44 molecular cloud in the CO $J = 3$–2 line (345.795 GHz) using the Atacama Submillimeter Telescope Experiment (ASTE) 10 m telescope. The observations were conducted in 2011 June and November. The telescope has a beam efficiency of 0.6 and an FWHM beam size of $22''$ at 345 GHz. The pointing of the telescope was checked and corrected every 2 hr by observing R Aql, and its accuracy was maintained within $2''$ (rms). The observations were made with a waveguide-type sideband-separating SIS mixer receiver CAT345 in the OTF mapping mode. The reference position was taken at $(l, b) = (+33.^{\circ}75, -1.^{\circ}509)$. During the observations, the system noise temperatures ranged between 200 and 600 K (single sideband). The antenna temperature ($T_{\rm A}^*$) was obtained by the standard chopper-wheel technique.

We used the digital AC spectrometer MAC (Sunada et al. 2000) in the wide-bandwidth mode, which covers an instantaneous bandwidth of 512 MHz with a 0.5 MHz resolution. At 346 GHz, this bandwidth and resolution correspond to a 444 km s^{-1} velocity coverage and 0.43 km s^{-1} velocity resolution. The full extent of the W44 radio shell was mapped in the OTF mode. The obtained data were reduced using the NOSTAR reduction package. Linear baselines were subtracted from the spectra. We scaled the antenna temperature by multiplying it by 1.667 (= 1/0.6) to obtain the main-beam temperature $T_{\rm MB}$. The data were smoothed with a Bessel–Gaussian function and resampled onto an $8.''5 \times 8.''5 \times 1.0$ km s^{-1} regular grid. The rms noise level of the final map is 0.15 K in $T_{\rm MB}$ (1σ).

3. RESULTS

3.1. Spatial Structure

Figure 1 shows velocity-integrated maps of HCO^+ $J = 1$–0 and CO $J = 3$–2 emission. These maps cover the entire extent of the W44 SNR. The Very Large Array (VLA) radio continuum image at 20 cm with a spatial resolution of $15''$ (Jones et al. 1993) is also placed on the right side for comparison. In contrast to the widespread CO $J = 1$–0 distribution (Seta et al. 2004), the HCO^+ $J = 1$–0 and CO $J = 3$–2 lines exhibit filamentary structure along with the radio continuum filaments of W44. The HCO^+ $J = 1$–0 emission comes mainly from the area of the W44 radio shell, whereas the faint CO $J = 3$–2 emission is spread over the GMC in the Galactic southeast of the shell. At $(l, b) = (+34.^{\circ}57, -0.^{\circ}43)$, another clump appears in both maps. This clump has a velocity of $V_{\rm LSR} \simeq +55$ km s^{-1}, which differs slightly from that of the associated GMC in the southeast. This corresponds to the feature labeled C11 in Seta et al. (2004).

3.2. Velocity Structure

Figure 2 shows longitude–velocity maps of the HCO^+ $J = 1$–0 and CO $J = 3$–2 emission. The wide band and extensive mapping data are combined to produce the HCO^+ longitude–velocity map. The broad velocity width feature at $(l, b) = (34.^{\circ}763, -0.^{\circ}524)$ is Wing 3 in Seta et al. (2004). In addition to the previously detected wings, we discovered faint, spatially extended wing emission in both the HCO^+ $J = 1$–0 and CO $J = 3$–2 lines. This extensive wing component completely overlaps the W44 radio shell and is therefore regarded as molecular gas shocked and disturbed by the SN blast wave. This situation is well illustrated by Figure 3(a), which shows the spatial distribution of the velocity dispersion calculated with the HCO^+ $J = 1$–0 data. The velocity dispersion exceeds 10 km s^{-1} only toward the radio shell, showing the spatial distribution of the extensive wing component.

We also show the spatial distribution of the average velocity calculated using the HCO^+ $J = 1$–0 data (Figure 3(b)). The average velocity changes systematically from the edge to the center of the W44 radio shell. The typical velocity at the southeastern edge is $V_{\rm LSR} \simeq +45$ km s^{-1}, and that toward the center is $\simeq +35$ km s^{-1}; thus, the velocity difference is ~ 10 km s^{-1}. This velocity gradient from the edge to the center might be due to the expansion of the shocked gas. In other words, shocked gas adjacent to the W44 SNR might be expanding at a velocity of $\sim$10 km s^{-1}.

3.3. Ultra-high-velocity Wing

At $(l, b) = (+34.^{\circ}73, -0.^{\circ}47)$, we noticed another high-velocity wing emission component in the CO $J = 3$–2 line with a velocity width of $\sim$90 km s^{-1}. Figures 4(a) and (b) show the spatial and longitude-velocity distributions of this ultra-high-velocity wing emission. The spatial size of this wing is very compact, ~ 0.5 pc. It arises from the main GMC component at $V_{\rm LSR} \simeq +40$ km s^{-1}, as the other "normal" wings do, extending toward negative velocities to $V_{\rm LSR} = -70$ km s^{-1}. Its velocity extension, $\Delta V \sim 100$ km s^{-1}, is far larger than that of the other wing emission detected in the W44 GMC. Figure 4(c) shows lines profiles of CO $J = 3$–2 and HCO^+ $J = 1$–0 toward the ultra-high-velocity wing. The HCO^+ profile is made from the extensive mapping data, since the wide-band mapping unfortunately does not cover it.

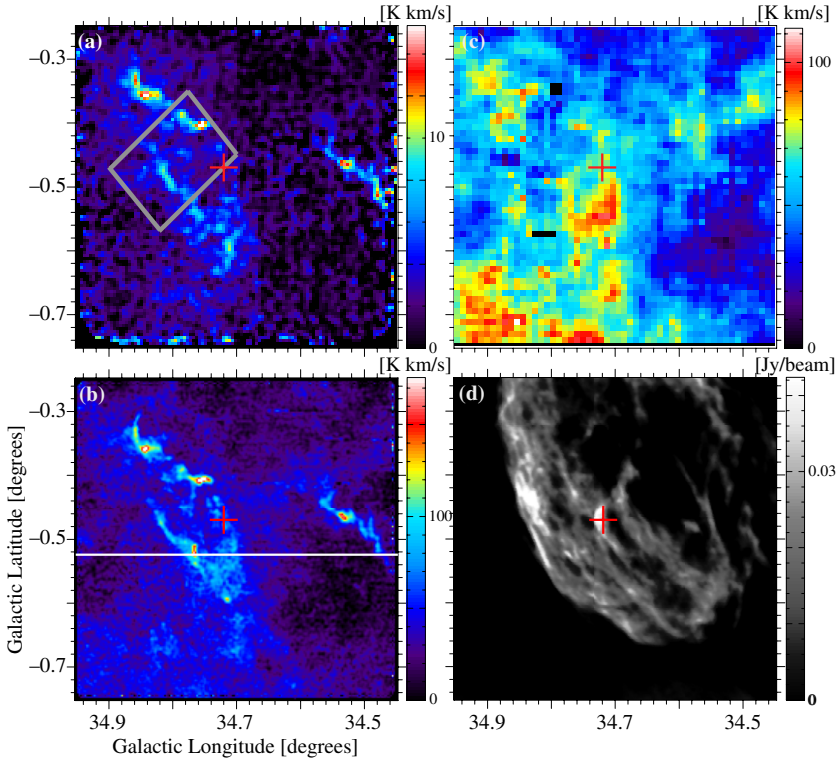

Figure 1. (a) Map of velocity-integrated HCO^+ $J = 1$–0 emission. The rectangle indicates the area where wide-band observations were performed. (b) Map of velocity-integrated CO $J = 3$–2 emission. The white solid line indicates $b = -0.^\circ524$, where the longitude–velocity maps are shown in Figure 2. (c) Map of velocity-integrated CO $J = 1$–0 emission. The velocity range of integration extends from $V_{LSR} = +20$ km s^{-1} to +60 km s^{-1} for images (a)–(c). (d) VLA radio continuum map at a wavelength of 20 cm (Jones et al. 1993). The red cross in each panel indicates the position of the ultra-high-velocity wing emission (Section 3.3).

(A color version of this figure is available in the online journal.)

Despite the great significance of the ultra-high-velocity wing, its nature is somewhat controversial. Spatially, it is intermingled with the extended wing emission. A prominent blob of radio continuum emission seems to be associated with this wing (Figure 1(d)). A nebulosity of the H_2 2.12 μm line emission also overlaps this wing (Figure 8 of Reach et al. 2005). These strongly suggest a close physical relationship between the ultra-high-velocity wing and the W44 SNR. More research is necessary to reveal the origin of this peculiar wing emission.

4. DISCUSSION

4.1. Velocity Components

Detection of the extensive wing enables us to analyze the kinematics of shocked molecular gas adjacent to the W44 SNR. As we saw in the previous section, its kinematics seem to be roughly reproduced by a simple expansion model. Before analyzing the kinematics, we inspected the line profiles in each line to extract the high-velocity wing component correctly. Hereafter, we refer to the high-velocity wing data as the "wing" and to the data remaining after the wing is subtracted from the original data as "non-wing data." The HCO^+ and CO data sets were analyzed separately.

Figure 5 shows profiles of the HCO^+ $J = 1$–0 and CO $J = 3$–2 lines toward $(l, b) = (34.^\circ82, -0.^\circ47)$. The HCO^+ $J = 1$–0 line profiles suffer from absorption or additional emission at $V_{LSR} = +46$ km s^{-1} from the foreground quiescent gas, which mainly belongs to the associated GMC. We used the original HCO^+ data as the wing since the restoration of unabsorbed profiles was difficult. In the CO $J = 3$–2 line profiles, the quiescent gas appears as narrow- or moderate-velocity-width emission. We referred to the CO $J = 1$–0 data to subtract this quiescent gas component. The subtracted main-beam temperature is expressed as $T_{MB}(3\text{–}2) - \xi T_{MB}(1\text{–}0)$, where ξ is the ratio between the total CO $J = 3$–2 and CO $J = 1$–0 intensities for quiescent gas ($\xi = 0.57$). We used the subtracted data as the CO $J = 3$–2 wing and thus the $\xi T_{MB}(1\text{–}0)$ data became non-wing data.

4.2. Expansion Model

We employed a simple expansion model to describe the kinematics of the shocked gas. The model consists of gas on the surface of a uniformly-expanding prolate ellipsoid. The center of the ellipsoid was taken to be $(l, b) = (34.^\circ65, -0.^\circ39)$ and the position angle with respect to the Galactic plane was taken to be 70°. The line-of-sight velocity can be written as

$$V_{los} = \begin{cases} V_{sys} + V_{exp}\sqrt{1 - s(x,y)^2} & [s(x,y) \leqslant 1] \\ V_{sys} & [s(x,y) > 1]\,, \end{cases} \quad (1)$$

where V_{sys} is the systemic velocity and V_{exp} is the expansion velocity. Further, $s(x, y)$ is the normalized projected distance from the center, defined as

$$1 - s(x,y)^2 \equiv \frac{1 - \left(\frac{x}{a}\right)^2 - \left(\frac{y}{b}\right)^2}{1 + \frac{a^2 - b^2}{a^2 b^2} x^2}, \quad (2)$$

where a and b are the semimajor and semiminor axes of the ellipsoid, respectively, and x and y are the projected distances from the center along the major and minor axes in the plane of

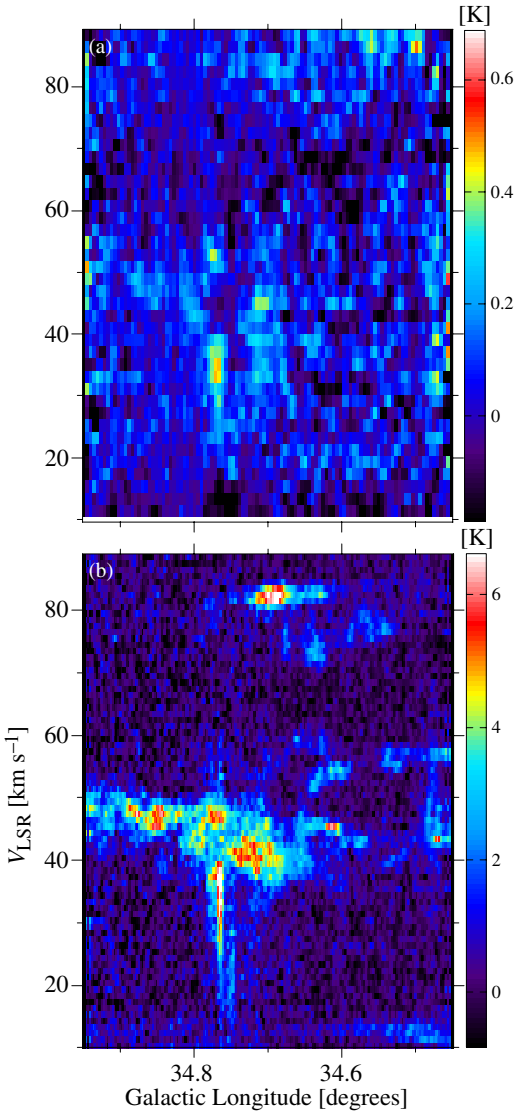

Figure 2. (a) Longitude–velocity map of HCO^+ $J = 1$–0 emission at $b = -0.^\circ524$. The intense broad-line-width feature at $l = 34.^\circ763$ is Wing 3 (Seta et al. 2004). We also see a faint broad-line-width feature at $(l, V_{LSR}) = (34.^\circ68$ to $34.^\circ76, +15$ km s^{-1} to $+55$ km s$^{-1})$. (b) Longitude–velocity map of CO $J = 3$–2 emission. The latitude is the same as for panel (a). Wing 3 and faint, spatially extended wing emission are apparent.

(A color version of this figure is available in the online journal.)

the sky, respectively. We employed $a = 0.^\circ30$ and $b = 0.^\circ21$ for the expanding shell of W44.

The average velocity toward each position was calculated with each data set using

$$\langle V \rangle = \int_{V_{min}}^{V_{max}} T_{MB} V dV \Big/ \int_{V_{min}}^{V_{max}} T_{MB} dV. \quad (3)$$

The limits of integration were chosen to be $V_{min} = +20$ km s^{-1} and $V_{max} = +60$ km s^{-1}. The systemic velocity was fixed at $V_{sys} = 47.5$ km s^{-1}, which is the average velocity of the HCO^+ and CO data at $s > 1$. Figures 6 and 7(a) show $\langle V \rangle$–$s(x, y)$ plots for HCO^+ and for the CO wing data. A standard least-squares fitting procedure yielded $V_{exp} = 12.2 \pm 0.3$ km s^{-1} for HCO^+ and $V_{exp} = 13.2 \pm 0.2$ km s^{-1} for the CO wing data. We employ an average value weighted by $1/\sigma^2$: $V_{exp} = 12.9 \pm 0.2$ km s^{-1}.

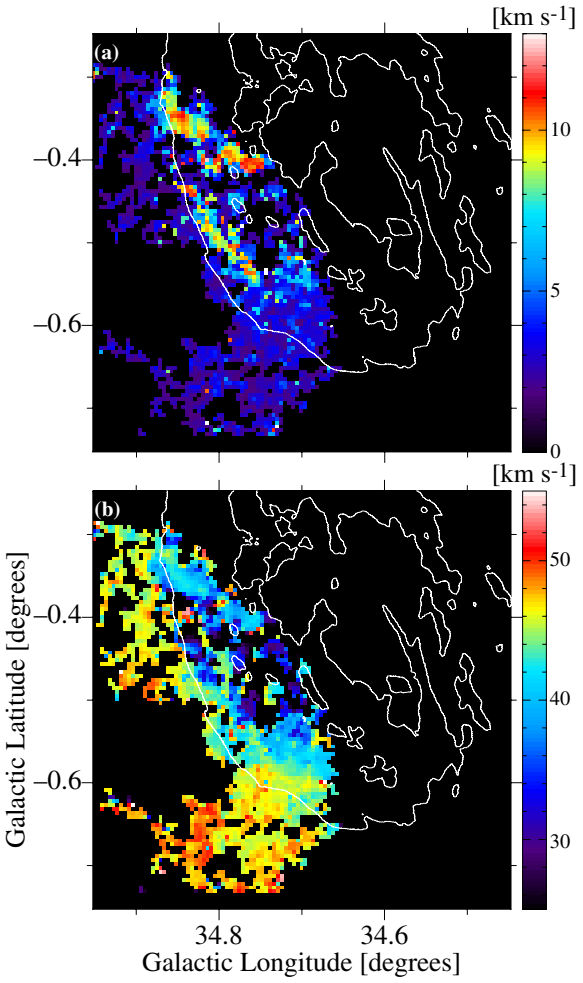

Figure 3. (a) Map of the velocity dispersion calculated with the HCO^+ $J = 1$–0 data. (b) Map of the average velocity calculated with the HCO^+ $J = 1$–0 data. Thick gray lines trace the outline of the W44 radio shell.

(A color version of this figure is available in the online journal.)

4.3. Kinetic Energy

The mass of the shocked gas M_s was estimated from the HCO^+ $J = 1$–0 intensity because it traces mostly shocked gas. We assumed that the line is optically thin and that the rotational levels are in local thermodynamic equilibrium (LTE) at $T_k = 40$ K. We employed the abundance ratio $[HCO^+]/[H_2] = (2.9 \pm 1.5) \times 10^{-9}$, which is the average value for Galactic molecular clouds (Ungerechts et al. 1997; Liszt & Lucas 2000). We obtained $M_s = (1.2 \pm 0.6) \times 10^4\ M_\odot$, where the error includes the intensity calibration uncertainty (~10%). Note that the estimated mass includes the SEMBE gas since we did not subtract the non-wing component from the HCO^+ data.

Because of the finite optical depth $[\tau(HCO^+) \sim 1]$, M_s is revised upward by a factor of two, whereas the subthermal conditions decrease it by a factor of several. For instance, a large velocity gradient (LVG) analysis with $n(H_2) = 10^5$ cm^{-3}, $T_k = 40$ K, and $\tau(HCO^+) \ll 1$ yields $M_s = (3.6 \pm 1.9) \times 10^3\ M_\odot$, which is 1/3 of the LTE estimation. Since these effects cancel to some extent, we employed the LTE estimation in the following discussion. The mass of shocked gas is a factor of four larger than that of the SEMBE, ~3000 $M_\odot$, which was estimated from the CO $J = 1$–0 data assuming $T_k = 20$ K (Seta et al. 2004).

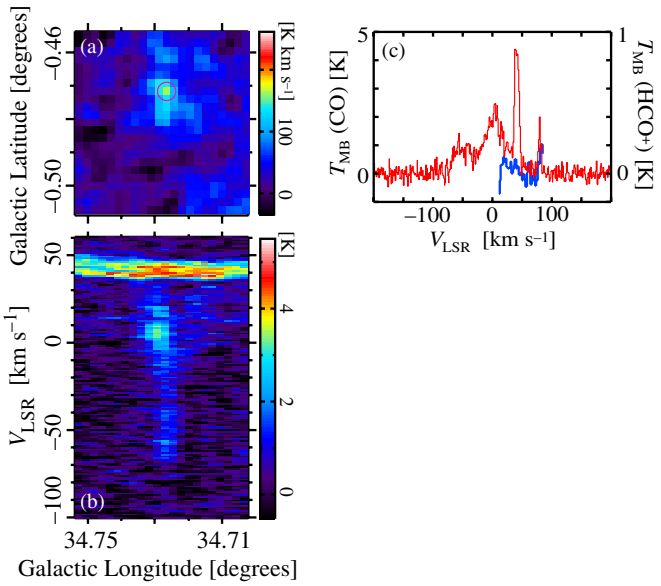

Figure 4. (a) Map of CO $J = 3$–2 emission integrated over velocities from −70 km s^{-1} to +30 km s^{-1}. The magenta circle indicates the area where the panel (c) spectra were created. (b) Longitude–velocity map of CO $J = 3$–2 emission at $b = -0.^{\circ}472$. (c) Line profiles of CO $J = 3$–2 (red) and HCO$^+$ $J = 1$–0 (blue) toward the ultra-high-velocity wing at $(l, b) = (+34.^{\circ}727, -0.^{\circ}472)$. Both spectra correspond to the emission smoothed spatially with a half-power beam width of 20″ Gaussian. The HCO$^+$ profile is from the extensive mapping data.

(A color version of this figure is available in the online journal.)

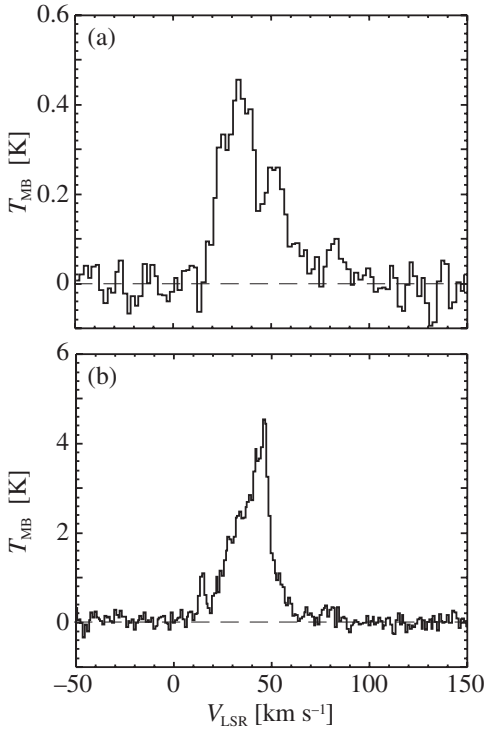

Figure 5. Line profiles of (a) HCO$^+$ $J = 1$–0 and (b) CO $J = 3$–2 toward $(l, b) = (+34.^{\circ}82, -0.^{\circ}47)$. The velocity resolutions are 1.7 km s^{-1} and 0.43 km s^{-1} for HCO$^+$ and CO, respectively.

The kinetic energy of the molecular gas provided by the SN blast wave consists of two terms:

$$E_{\rm kin}({\rm mol}) = E_{\rm exp} + E_{\rm turb} = \frac{1}{2}M_{\rm s}V_{\rm exp}^2 + \frac{3}{2}M_{\rm s}\left(\sigma_{\rm s}^2 - \sigma_{\rm q}^2\right). \quad (4)$$

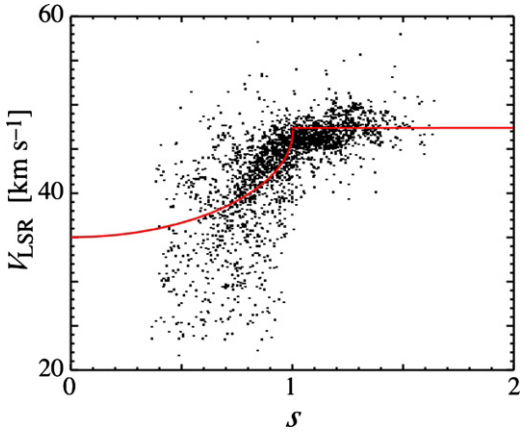

Figure 6. Average velocity vs. normalized distance [$\langle V\rangle$–$s(x, y)$] calculated with the HCO$^+$ $J = 1$–0 wing data.

(A color version of this figure is available in the online journal.)

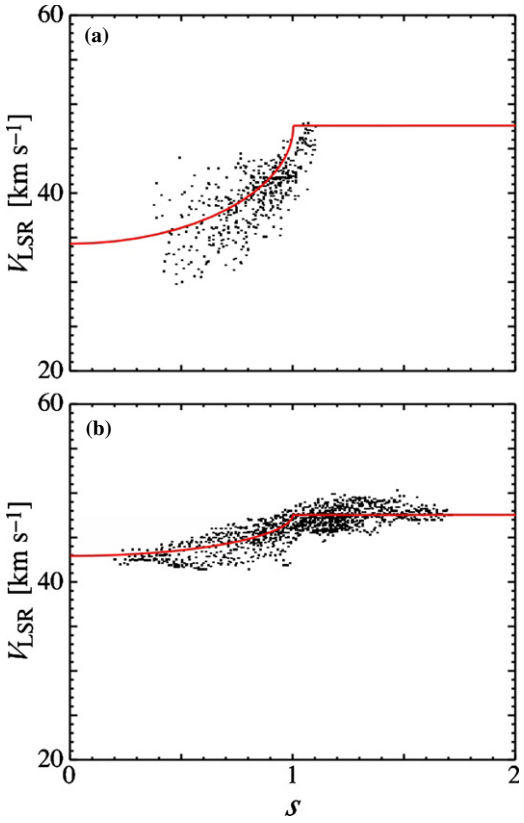

Figure 7. (a) Plot of average velocity vs. normalized distance [$\langle V\rangle$–$s(x, y)$] calculated with the CO $J = 3$–2 "wing" data. (b) The $\langle V\rangle$–$s(x, y)$ plot for the CO $J = 3$–2 "non-wing" data.

(A color version of this figure is available in the online journal.)

The first term is the expansion energy and the second term corresponds to the increase in the turbulent energy, where $\sigma_{\rm s}$ ($\sigma_{\rm q}$) is the one-dimensional velocity dispersion of the shocked (quiescent) gas. We obtained $\sigma_{\rm s} = 6.8 \pm 0.1$ km s^{-1} and $\sigma_{\rm q} = 2.30 \pm 0.02$ km s^{-1} using the wing and non-wing data for the CO $J = 3$–2 line, respectively. Thus, we obtained $E_{\rm exp} = (2.0 \pm 1.1) \times 10^{49}$ erg and $E_{\rm turb} = (1.5 \pm 0.8) \times 10^{49}$ erg, and thus $E_{\rm kin}({\rm mol}) = (3.5 \pm 1.3) \times 10^{49}$ erg for the shocked molecular gas.

In addition to the shocked molecular gas, an H I expanding shell is associated with the W44 SNR (Koo & Heiles 1995).

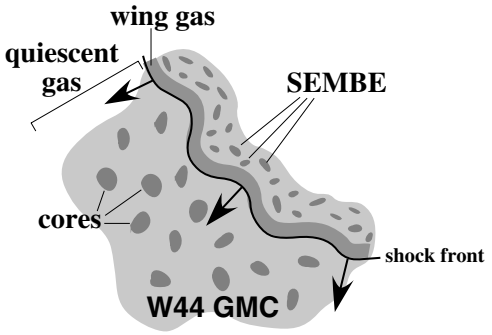

Figure 8. Schematic view of the W44 blast wave based on our HCO$^+$ $J = 1$–0 and CO $J = 3$–2 observations. Non-wing gas is the mixture of quiescent and SEMBE gas.

Since this H I shell was detected with positive high velocities, it covers the far-side portion of the W44 SNR, while the GMC covers the near side. The lower limit to the total kinetic energy provided by the SNR is given by adding the kinetic energy of the H I shell, $(8.0 \pm 1.0) \times 10^{49}$ erg, to $E_{\rm kin}$(tot), which yields $(1.2 \pm 0.2) \times 10^{50}$ erg. On the other hand, the W44 GMC covers approximately one-fourth of the radio shell in the plane of the sky. Thus, the upper limit might be obtained by extrapolating $E_{\rm kin}$(mol) to the entire solid angle by multiplying by 8, which yields $(2.8 \pm 1.1) \times 10^{50}$ erg.

The kinetic energies obtained above correspond to a conversion efficiency of $\eta = (0.1$–$0.3)(E_{\rm bar}/10^{51}\ {\rm erg})^{-1}$. This is in good agreement with the prediction of an early theoretical study (Chevalier 1974) if the SN baryonic energy does not differ significantly from 10^{51} erg. Note that the estimated upper and lower limits and the theoretical prediction are all compatible, despite uncertainties in our basic assumptions.

4.4. The Relation between the Wing and the SEMBE

We analyzed the CO $J = 3$–2 non-wing data in the same way as the wing data. Figure 7(b) shows a $\langle V \rangle$–$s(x, y)$ plot for the CO $J = 3$–2 non-wing data. A velocity gap at $s \simeq 1$ is apparent, and the behavior of $\langle V \rangle$ is explained well by an expansion model. A least-squares fit yields $V_{\rm exp} = 4.7 \pm 0.1$ km s^{-1} for the non-wing gas. This result indicates that the non-wing gas is not totally quiescent and that most of it is affected by the SNR. This non-wing expanding gas might correspond to the SEMBE of the CO $J = 1$–0 line (Seta et al. 2004).

Although the nature of the SEMBE is still controversial, its spatial distribution suggests that it is related to the blast wave of the W44 SNR. The expansion of the non-wing gas might support this notion. Its slow expansion and moderately broad velocity width indicate that it is located downstream of the wing-emitting gas with respect to the shock front. Most likely, it was a higher-density region before the passage of the SN blast wave because high-density gas decelerates shock waves. A simple Sedov solution indicates that the expansion velocity is proportional to $(E/\rho)^{0.2}\, t^{-0.6}$, where t is the elapsed time from the explosion. Thus, a preshock density that is higher by a factor of 240 decreases the expansion velocity by a factor of 3.

Figure 8 shows a schematic view of the shocked gas adjacent to the W44 SNR. We hypothesize that the precursor of the SEMBE gas consisted of a number of unresolved dense clumps embedded in the W44 GMC. These dense clumps decelerated the SN blast wave, distorted the shock front, and thereby were left behind it. The SEMBE is barely detected in HCO$^+$ with $T_{\rm MB} \lesssim 0.2$ K. The complex configuration of the SEMBE gas, wing-emitting gas, and foreground quiescent gas generates the various observed shapes of the HCO$^+$ $J = 1$–0 profiles.

The size of the putative dense clumps must be far smaller than 0.3 pc in diameter, since they are unresolved by a $\sim$20″ beam. An LVG analysis with $n({\rm H_2}) = 3 \times 10^4$ cm^{-3}, $T_{\rm k} = 20$ K, [HCO$^+$]/[H$_2$] $= 2.9 \times 10^{-9}$, and $T_{\rm MB}$(HCO$^+$) $= 0.2$ K gives $N({\rm H_2})/dV = 1.6 \times 10^{20}$ cm^{-2} (km s^{-1})$^{-1}$. This column gives $T_{\rm MB}$(CO 1–0) $\simeq 8$ K, which is typical for the SEMBE, if we assume [CO]/[H$_2$] $= 8 \times 10^{-5}$. Using $dV = 5$ km s^{-1}, the size of dense clumps in the SEMBE is estimated to be $\sim 8 \times 10^{-3}$ pc (0.″6 at 3 kpc). ALMA may be able to resolve such small clumps at mm-wavelengths.

Moderately broad ($\Delta V = 7.5$ km s^{-1}) CO emission was also detected from the SNR G18.8+0.3 (Dubner et al. 2004). This could be another example of the SEMBE. More SEMBE detections could be made from careful inspection of the existing CO data and by sensitive molecular line observations toward SNR–MC interacting systems (e.g., Table 2 in Jiang et al. 2010). Direct imaging of the dense clumps responsible for the SEMBE using millimeter and submillimeter arrays will be essential for examining the SEMBE model.

5. CONCLUSION

Observations from the NRO 45 m and ASTE 10 m telescopes toward the GMC associated with W44 yielded the following conclusions:

1. Extensive HCO$^+$ $J = 1$–0 and CO $J = 3$–2 maps delineated the distribution and kinematics of shocked molecular gas adjacent to the W44 SNR.
2. The average velocity distributions of the shocked gas can be fit by a uniform expansion model. The best-fit expansion velocities are 12.2 ± 0.3 km s^{-1} and 13.2 ± 0.2 km s^{-1} in HCO$^+$ and CO, respectively.
3. The non-wing CO $J = 3$–2 component is also fit by the same model with an expansion velocity of 4.7 ± 0.1 km s^{-1}. This component might be dominated by the SEMBE. The precursor of the SEMBE gas might be a number of unresolved dense clumps that decelerated the SN blast wave.
4. The estimated mass and kinetic energy of the shocked molecular gas are $M_{\rm s} = (1.2 \pm 0.6) \times 10^4\, M_\odot$ and $E_{\rm kin}({\rm mol}) = (3.5 \pm 1.3) \times 10^{49}$ erg, respectively.
5. After adding the energy of the H I shell, we concluded that at least $(1.2 \pm 0.2) \times 10^{50}$ erg has been converted into gas kinetic energy from the initial baryonic energy of the W44 SN. On the other hand, the upper limit on the energy available for disturbing interstellar matter is $(2.8 \pm 1.1) \times 10^{50}$ erg.
6. We also found ultra-high-velocity CO $J = 3$–2 wing emission with a velocity width of $\sim$100 km s^{-1} at $(l, b) = (+34.^\circ73, -0.^\circ47)$. The origin of this extremely high velocity wing is quite mysterious.

We are grateful to the NRO staff for their excellent support of the 45 m observations. The Nobeyama Radio Observatory is a branch of the National Astronomical Observatory of Japan, National Institutes of Natural Sciences. We thank the members of the ASTE team for the operation of the telescope and ceaseless efforts to improve the ASTE. Observations with ASTE were conducted remotely from the NRO using NTT's GEMnet2 and its partner R&E (Research and Education) networks, which are based on the AccessNova collaboration

between the University of Chile, NTT Laboratories, and the National Astronomical Observatory of Japan. We also thank the anonymous referee for helpful comments and suggestions that improved the manuscript. This work is partially supported by JSPS Grant-in-Aid for Scientific Research(C) No. 24540236.

REFERENCES

Caswell, J. L., Murray, J. D., Roger, R. S., Cole, D. J., & Cooke, D. J. 1975, A&A, 45, 239
Chevalier, R. A. 1974, ApJ, 188, 501
Clark, D. H., Green, A. J., & Caswell, J. L. 1975, AuJPA, 37, 75
Claussen, M. J., Frail, D. A., Goss, W. M., & Gaume, R. A. 1997, ApJ, 489, 143
Claussen, M. J., Goss, W. M., Frail, D. A., & Desai, K. 1999, ApJ, 522, 349
Dubner, G., Giacani, E., Reynoso, E., & Parón, S. 2004, A&A, 426, 201
Frail, D. A., & Mitchell, G. F. 1998, ApJ, 508, 690
Gronenschild, E. H. B. M., Mewe, R., Heise, J., et al. 1978, A&A, 65, L9
Harrus, I. M., Hughes, J. P., Singh, K. P., Koyama, K., & Asaoka, I. 1997, ApJ, 488, 781
Jiang, B., Chen, Y., Wang, J., et al. 2010, ApJ, 712, 1147
Jones, L. R., Smith, A., & Angelini, L. 1993, MNRAS, 265, 631
Kassim, N. 1992, AJ, 103, 943
Koo, B.-C., & Heiles, C. 1995, ApJ, 442, 679
Kundu, M. R., & Velusamy, T. 1972, A&A, 20, 237
Liszt, H., & Lucas, R. 2000, A&A, 355, 333
Radhakrishnan, V., Goss, W. M., Murray, J. D., & Brooks, J. W. 1972, ApJS, 24, 49
Reach, W. T., Rho, J., & Jarrett, T. H. 2005, ApJ, 618, 297
Reich, W., Fuerst, E., Haslam, C. G. T., Steffen, P., & Reif, K. 1984, A&AS, 58, 197
Rho, J., Petre, R., Schlegel, E. M., & Hester, J. J. 1994, ApJ, 430, 757
Seta, M., Hasegawa, T., Dame, T. M., et al. 1998, ApJ, 505, 286
Seta, M., Hasegawa, T., Sakamoto, S., et al. 2004, AJ, 127, 1098
Smith, A., Jones, L. R., Watson, M. G., et al. 1985, MNRAS, 217, 99
Strickland, D. K., & Heckman, T. M. 2009, ApJ, 697, 2030
Sunada, K., Yamaguchi, C., Nakai, N., et al. 2000, Proc. SPIE, 4015, 237
Ungerechts, H., Bergin, E. A., Goldsmith, P. F., et al. 1997, ApJ, 482, 245